Surface phase, morphology, and charge distribution transitions on vacuum and ambient annealed SrTiO_{3}(100)

Omur E. Dagdeviren, Georg H. Simon, Ke Zou, Fred J. Walker, Charles Ahn, Eric I. Altman, and Udo D. Schwarz

Phys. Rev. B **93**, 195303 — Published 4 May 2016

DOI: 10.1103/PhysRevB.93.195303

Surface Phase, Morphology, and Charge Distribution Transitions on Vacuum and Ambient Annealed $SrTiO_3$ (100)

Omur E. Dagdeviren,[1,2] Georg H. Simon,[1,2] Ke Zou,[2,4] Fred J. Walker,[2,4] Charles Ahn,[1,2,4] Eric I. Altman,[2,3] and Udo D. Schwarz[1,2,3*]

[1]Department of Mechanical Engineering and Materials Science, Yale University, New Haven, CT 06520, USA

[2]Center for Research on Interface Structures and Phenomena (CRISP), Yale University, New Haven, CT 06520, USA

[3]Department of Chemical and Environmental Engineering, Yale University, New Haven, CT 06520, USA

[4]Department of Applied Physics, Yale University, New Haven, CT 06520, USA

[*]Corresponding author: udo.schwarz@yale.edu

Keywords: strontium titanate ($SrTiO_3$), scanning probe microscopy, scanning probe spectroscopy, Auger electron spectroscopy, low-energy electron diffraction

Abstract

The surface structures of $SrTiO_3$ (100) single crystals were examined as a function of annealing time and temperature in either oxygen atmosphere or ultra-high vacuum (UHV) using noncontact atomic force microscopy (NC-AFM), Auger electron spectroscopy (AES), and low-energy electron diffraction (LEED). Samples were subsequently analyzed for the effect the modulation of their charge distribution had on their surface potential. It was found that the evolution of the $SrTiO_3$ surface roughness, stoichiometry, and reconstruction depends on the preparation scheme. LEED revealed phase transitions from a (1×1) termination to an intermediate c(4×2) reconstruction to ultimately a (√13×√13)-*R*33.7° surface phase when the surface was annealed in an oxygen flux, while the reverse transition from (√13×√13)-*R*33.7° to c(4×2) was observed when samples were annealed in UHV. When the surface reverted to c(4×2), AES data indicated decreases in both the surface Ti and O concentrations. These findings were corroborated by NC-AFM imaging, where initially TiO_2-terminated crystals developed half unit cell high steps following UHV annealing, which is typically attributed to a mix of SrO and TiO_2 terminations. Surface roughness evolved non-monotonically with UHV annealing temperature, which is explained by electrostatic modulations of the surface potential caused by increasing oxygen depletion. This was further corroborated by experiments in which the apparent roughness tracked in NC-AFM could be correlated with changes in the surface charge distribution that were controlled by applying a bias voltage to the sample. Based on these findings, it is suggested that careful selection of preparation procedures combined with application of an electric field may be used to tune the properties of thin films grown on $SrTiO_3$.

1. Introduction

The structure and properties of strontium titanate ($SrTiO_3$) have attracted substantial interest in the past due to the material's popularity as a substrate for complex oxide epitaxy,[1-3] a status it owes to its near perfect lattice match to a number of frequently used materials such as $PbZr_{0.52}Ti_{0.48}O_3$ (PZT), $La_{2/3}Ca_{1/3}MnO_3$ (LCMO), and $SrRuO_3$.[3-8] In addition, FeSe thin films grown on $SrTiO_3$ have recently attracted attention due to their display of interfacial high temperature superconductivity, which has been associated with charge transfer to FeSe from Ti^{+3} formed by surface reduction.[9-13] Ultimately, such studies attempt to enable improvements in device quality by correlating the physical properties of devices made from thin film heterostructures to the specifics of the bare substrate's surface termination, structure, and chemical state. Progress, however, has been hampered by the richness of phenomena and surface states that may manifest depending on the surface's exact preparation procedures.

Strontium titanate crystallizes in a cubic perovskite structure with a 3.905 Å lattice parameter and a unit cell that features equidistant alternating SrO and TiO_2 layers along <100> directions. Since both layers are thermodynamically stable and non-polar, a (100) surface in principle can expose either of the two terminations, making the properties of the surface a local characteristic.[14-23] Given that SrO- and TiO_2-terminated terraces differ substantially in their chemical and electrical properties,[14,24-29] the characteristics of films grown on nominally mixed-terminated substrates will vary locally as well. Similar to many other perovskite metal oxides, $SrTiO_3$ commonly reconstructs; the plethora of reconstructions identified include (2×1), (2×2), (4×4), c(4×2), c(4×4), c(6×2), (√5×√5)-*R*26.6°, and (√13×√13)-*R*33.7° structures.[16,18,20,24,26,30-46] Which reconstruction, or combination of reconstructions, is encountered in any given case depends crucially on details of the surface preparation procedure.[18,19,41,43,44,47,48] An

understanding and characterization of these surface states – and the procedures that lead to them – is nevertheless important as they affect the properties of any $SrTiO_3$/thin film interface grown on them. Transformations from one reconstruction to another are mainly governed by three parameters: temperature, annealing time, and the amount of oxygen offered during heating.[22,44,47,49] Understanding the possible phase trajectories is crucial to shed light on the thermodynamics and kinetics of these transformations.

In this article, we present a study of local $SrTiO_3$ surface properties as a function of preparation history by noncontact atomic force microscopy (NC-AFM)[50-53] with complementary data on the macroscopic surface phase transitions via low energy electron diffraction (LEED) and the accompanying changes in surface composition via Auger electron spectroscopy (AES). While the majority of prior studies have focused on reducing environments, in part because their surface analysis techniques require reduction to achieve satisfactory conductivity, here the use of NC-AFM liberates us to examine the surface starting with near stoichiometric amounts of oxygen.[22,44,47,49] We observe that high O chemical potentials lead to surfaces terminated in a $(\sqrt{13}\times\sqrt{13})$-*R*33.7° reconstruction with double TiO_2 layers that evolve to less Ti-rich surface phases upon reduction, and that surface roughness shows a non-monotonic trend as a function of annealing temperature in UHV. Both phenomena can be connected to changes in surface composition and bulk oxygen deficiency. Our results highlight that not only the surface structure, but also the electrostatic surface potential changes as the material is oxidized and reduced. Since the charged defects move under the influence of an electric field, it may open a new route to controlling the properties of $SrTiO_3$ surfaces during thin film growth.

2. Experiments

Noncontact atomic force microscopy experiments were carried out in ultrahigh vacuum (UHV) at room temperature with a base pressure of below 2×10^{-10} mbar using a home-built microscope that has been described in detail elsewhere.[54] Probe tips were mechanically cut Pt/Ir wires in a qPlus configuration.[55,56] All NC-AFM data was recorded in *tuned-oscillator atomic force microscopy* (TO-AFM) mode, a recently developed operating scheme that simplifies data acquisition due to its use of only one feedback loop; for details, see.[57] All AES and LEED measurements presented in this paper were conducted using a second UHV system described in detail elsewhere.[58] Identical preparation steps were used in the two systems. To ensure the relevance of the LEED/AES data for interpreting NC-AFM measurements, we also performed LEED in the first system, which reproduced all findings from the second system.

Experiments were executed on samples from two different sources. The LEED data in Fig. 2d as well as the NC-AFM measurements shown in Figs. 4-6 were performed on 0.7 % Nb-doped $SrTiO_3$ crystals that were bought from MTI Cooperation, USA, etched in-house with a HCl (1 molar)/HNO_3 (3 molar) solution followed by rinsing with ethanol and acetone.[59] In contrast, the LEED/AES results Figs. 1, 2a-c, and 3 and the NC-AFM data Fig. 7 were obtained using undoped samples supplied by CrysTec GmbH, Germany. These samples were etched at the company using buffered HF solution. Both doped and updoped samples were subsequently annealed in 1 atm O_2 in a furnace at 1270 K for between 30 minutes to 10 hours (plus heat up and cool down times of 3 h each) and introduced to UHV within 10-15 minutes after cooling.

Vacuum annealing was carried out at pressures that never exceeded 8×10^{-10} mbar; note that five minutes for heating up and cooling down were added to the hold times specified for

each experiment. For NC-AFM experiments, the sample was allowed to equilibrate to room temperature for a couple of hours to minimize thermal drift, while AES and LEED measurements were commenced within 30 minutes of annealing. Finally, root mean square (rms) surface roughness data obtained on individual terraces as presented in Sects. 3.3 and 3.4 were obtained by averaging multiple values obtained on distinct 100 nm × 100 nm areas. Sampling a variety of surface locations and scan sizes confirmed that the values are asymptotically accurate (i.e., choosing larger areas did not statistically relevantly change the results).

3. Results

3.1 Characterization of Surface States with LEED and AES

To provide context for the NC-AFM results of sections 3.2-3.4, we first characterized the evolution of the surface structure and composition that can occur under a variety of preparation schemes with LEED and AES. The starting points were always etched surfaces with only (1×1) spots visible in LEED. Tracking the evolution of the LEED patterns as a function of annealing environment, temperature, and time revealed predominantly signatures of the c(4×2), (√13×√13)-*R*33.7°, and (4×4) reconstructions, examples of each are presented in Fig. 1. In addition, traces of (2×1) and (2×2) reconstructions mixed with combinations of c(4×2) and (4×4) were also observed. Note that the (2×2) reconstruction is difficult to distinguish from the (4×4) as the (2×2) pattern is a subset of the (4×4) termination; existence of the (2×2) is, however, hinted at by variations in the intensity of spots associated with both (2×2) and the (4×4) compared to spots associated with the (4×4) only.

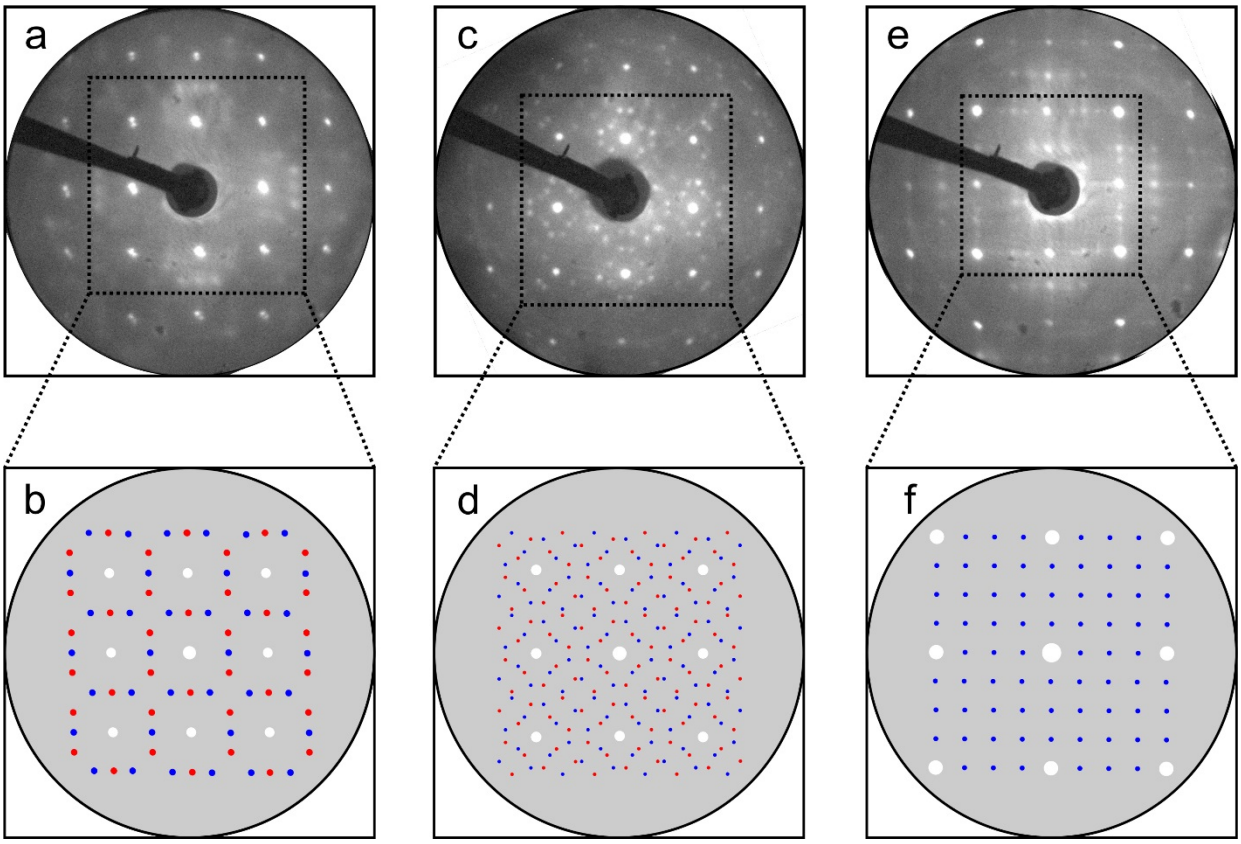

Figure 1: Selected LEED results representing the three main structures observed in tandem with their simulated LEED patterns: 1) c(4×2) phase (a), obtained after a 30 minute anneal in O_2 flux at 1270 K, and simulation (b). 2) ($\sqrt{13}\times\sqrt{13}$)-*R*33.7° phase (c), prepared by extending the anneal time to 10 hours, along with its simulated pattern (d). 3) (4×4) phase (e), obtained by sequential heating in UHV to first 900 K and then 950 K for 30 minutes each following a preparation as in 2), and its corresponding theoretical LEED pattern (f). All LEED patterns have been recorded at 130 eV beam energy. The white dots in b), d), and f) reflect the (1×1) periodicity, the blue dots the periodicities of the reconstructions, and the red dots in b) and d) rotationally equivalent domains of the reconstruction.

A phase map for the $SrTiO_3$ surface structure as a function of annealing environment, time, and temperature is presented in Fig. 2. In (a), we see that when annealed in a furnace under high purity O_2 flux at 1270 K, the original (1×1) pattern transforms first into a c(4×2)-reconstructed surface (30-minutes anneal; see panel a-i). Previous studies found this termination only after sputtering the samples with Ar followed by annealing;[20,22] our findings demonstrate

that this reconstruction is not due to preferential O sputtering or UHV annealing. Longer annealing times result in a slow transformation to a (√13 × √13)-*R*33.7° termination (mixed c(4×2)/ (√13×√13)-*R*33.7° phase after 5 hours, Fig. 2a-ii), which is fully established after about 10 hours (Fig. 2a-iii). This transformation after prolonged annealing suggests the (√13 × √13)-*R*33.7° reconstruction as the favored surface structure under oxidizing conditions. A qualitatively similar behavior, but with a longer time constant, was observed when the sample was removed from the O_2 furnace after 30 minutes, introduced into UHV (Fig. 2b-i), and then annealed at lower temperature (900 K) in 10^{-6} mbar O_2. Under these circumstances, traces of the c(4×2) phase were still visible even after 16 hours of continuous heating (Fig. 2b-iii). Nonetheless, the transition towards the (√13 × √13)-*R*33.7° reconstruction at lower temperatures in an O_2 background supports the assignment of this reconstruction as the favored phase at high oxygen chemical potentials. Others have found that annealing sputtered samples for shorter times or at different temperatures leads to either c(4×2) or (2×1) reconstructions.[18,22]

The c(4×2) → (√13×√13)-*R*33.7° transition could be roughly reversed when a sample featuring a crisp (√13×√13)-*R*33.7° pattern was annealed in UHV (Fig. 2c). Starting with Fig. 2c-i, after annealing at 900 K for 30 minutes, a (√13×√13)-*R*33.7°/c(4×2) mixed phase starts to appear (Figure 2 c-ii); applying an additional 30-minutes anneal at 950 K then morphs the surface's LEED pattern into a crisp pattern indicative of the c(4×2) reconstruction only (Figure 2 b-iii). Annealing at higher temperatures (Fig. 2c-iv: 30 minutes at 1000 K; Fig. 2c-v: additional 30 minutes at 1150 K) then gave rise to LEED signatures reflecting combinations of c(4×2), (4×4), (2×2), and (2×1) reconstructions. A qualitatively similar picture is obtained if we start the UHV anneal with a c(4×2)-terminated sample prepared as in Fig. 2a-i (Fig. 2d), but with slightly lower transformation temperatures. These results, whose intricacy is analogous to the complexity

observed on $BaTiO_3$(100), suggest that the ($\sqrt{13}\times\sqrt{13}$)-*R*33.7° is a particularly oxygen-rich reconstruction, while the c(4×2), (4×4), (2×2), and (2×1) are likely comparatively increasingly oxygen deficient.[23,33,44,47] For $BaTiO_3$ it has been shown that the observed progression between these reconstructions depends sensitively on the trajectory through the phase space.[47]

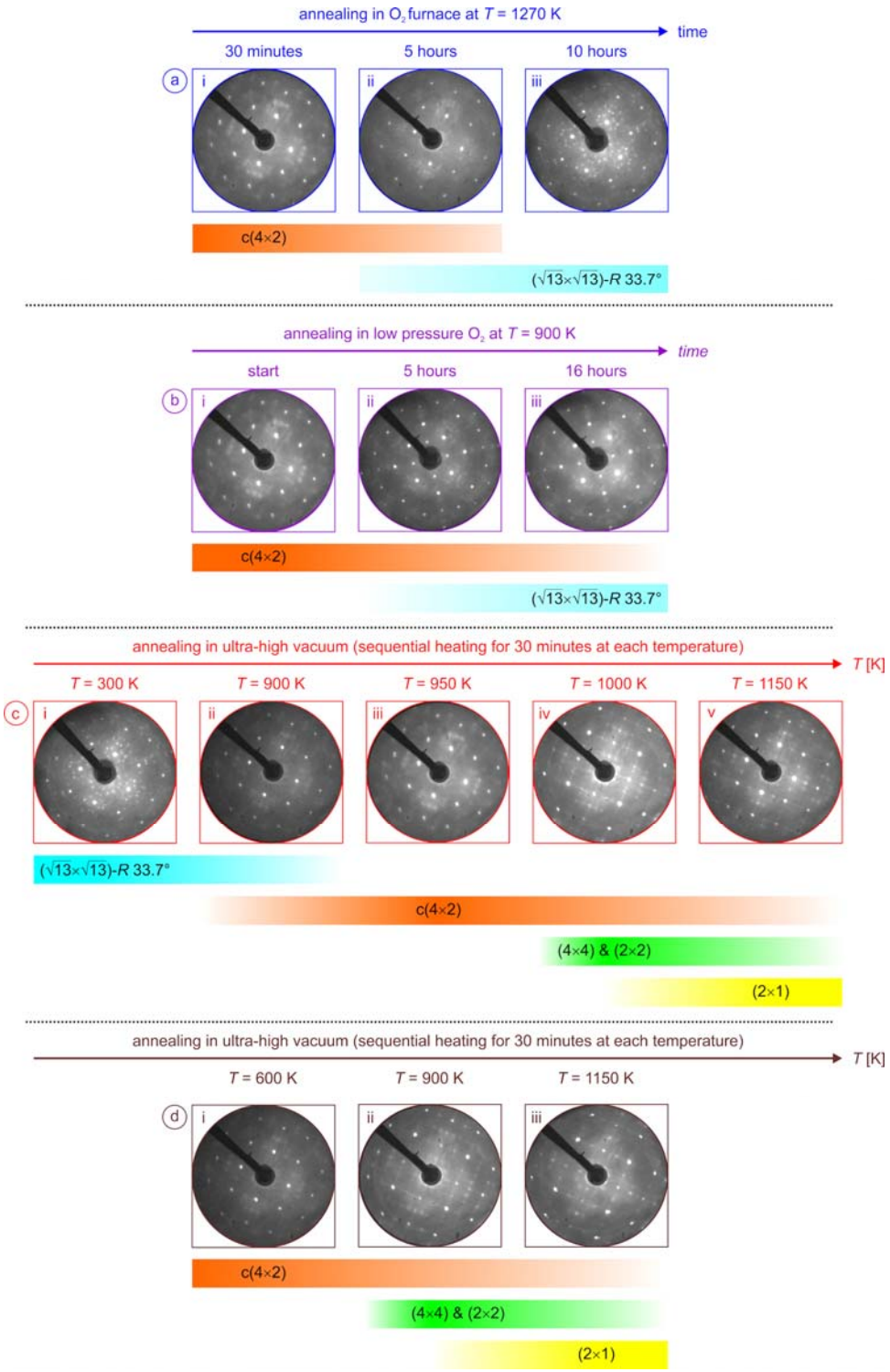

Figure 2: Structural phase transitions on $SrTiO_3$ (100) as a function of temperature, time, and environment. (a) Under continuous O_2 flux at T = 1270 K, LEED patterns evolve from 1×1 to c(4×2) and finally (√13×√13)-*R*33.7°. (b) If, after 30 min in O_2 flux, annealing is continued in UHV at a lower temperature (T = 900 K) and lower O_2 pressure (10^{-6} mbar), the same trend is

observed but with a longer time constant; the c(4×2) is still visible even after 16 hours of heating. (c) The transformation is reversed for annealing in UHV, where the c(4×2) reconstruction can be recovered from a (√13×√13)-*R*33.7°-terminated surface (c i-iii). Further annealing results in combinations of c(4×2), (4×4), (2×2), and (2×1) reconstructions (b iv-v). (d) When starting from a c(4×2)-reconstructed surface, the results are qualitatively similar to those in (c), but with the transformations at slightly lower temperatures.

For complementary insight into the nature of the phase transformations, we have characterized the surface by AES under conditions similar to the UHV anneal of Fig. 2c. The corresponding AES spectra are plotted in Fig. 3a for the as-introduced sample (sample preparation as for Fig. 2c-i) and for data obtained on the same sample after it had been heated to 600 K, 900 K, and 1000 K for 35 minutes each. To track the relative O, Sr, and Ti surface concentrations, for each spectrum we calculated first the ratio of the peak heights for Sr and Ti with respect to the peak height of oxygen and then calibrated the resulting values so that it reads one at T = 300 K ('normalized ratio'). Two conclusions can be deduced from the results: First, the increase of both the Sr and the Ti ratios with annealing temperature (Fig. 3b) confirm that oxygen is lost from the surface during the UHV anneal; and second, the higher slope for the Sr curve implies that the surface's Sr content increases relative to titanium. Considering that the starting (√13×√13)-*R*33.7° surface was previously found to be terminated by a double TiO_2 layer,[23] this does not mean that the surface after annealing is necessarily super-stoichiometric in Sr.[16,21,41,49]

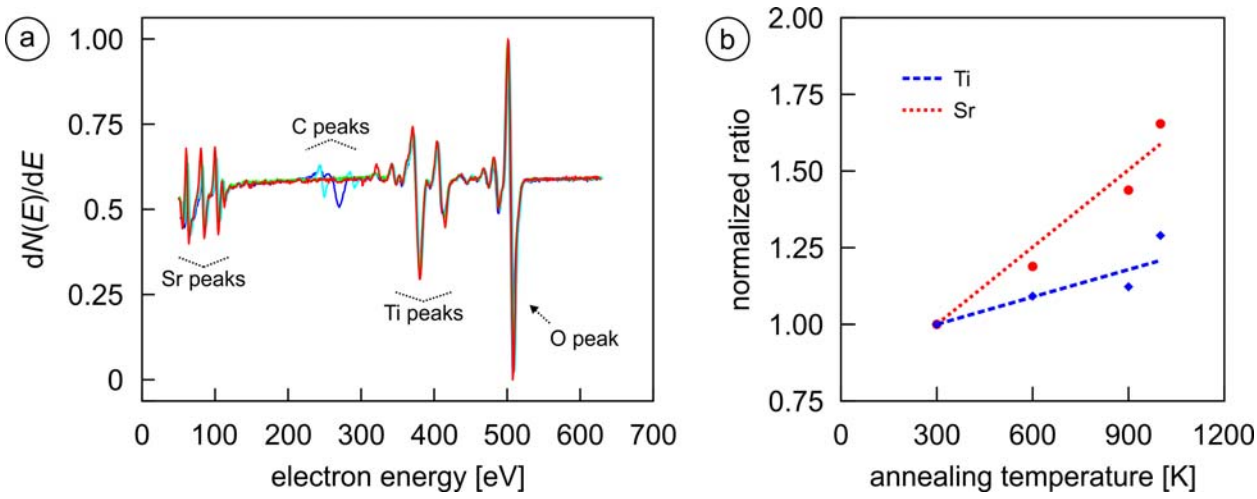

Figure 3: (a) AES derivative spectra obtained on the as-introduced sample (dark blue) as well as on the same sample after it had been heated to 600 K (light blue), 900 K (green), and 1000 K (red) for 35 minutes each; all spectra are normalized with respect to oxygen peak. Initial traces of carbon contamination are removed for annealing temperatures above 600 K. (b) Plot of the ratios of the Sr/O (red) and Ti/O (blue) peak heights with respect to their peak heights at T = 300 K. The data suggests that while the surface overall loses oxygen, the surface concentration of strontium increases relative to titanium. The error of the normalized ratio was determined to be ±5% while the uncertainty in the temperature reading was estimated at ±25 K.

3.2 Evolution of Surface Morphology

In the next step, we characterized the surface morphology of $SrTiO_3$(100) crystals by NC-AFM under various preparation conditions to investigate connections between terrace structures, surface roughness, and the trends uncovered by LEED and AES. Figure 4 shows results acquired on a sample prepared as in Fig. 2a-i (c(4×2) termination). After outgassing for 30 minutes at T = 470 K (Fig. 4a), we only find terraces separated by unit cell step height (3.905 Å; marked by the blue dotted lines), which implies that the surface is uniformly covered by the same termination.[16,20,25] Interestingly, after annealing (Fig. 4b-d), steps with fractional step height are found (2 Å: green dotted lines; 6 Å: red dotted lines), which predominantly follow the crystallographic [010] and [001] directions. Further annealing at 1170 K causes a greater diversity in step heights, with some even larger than 6 Å; in addition, ≈2 Å deep holes were

observed. Non-integer unit cell step heights are typically attributed to terminating the crystal at each of the two possible layers of the perovskite structure. [16,49] In addition to alternate surface terminations, fractional step heights can also result from organization of bulk defects into planes or from segregation of a non-stoichiometric surface layer.[30,49,60,61]

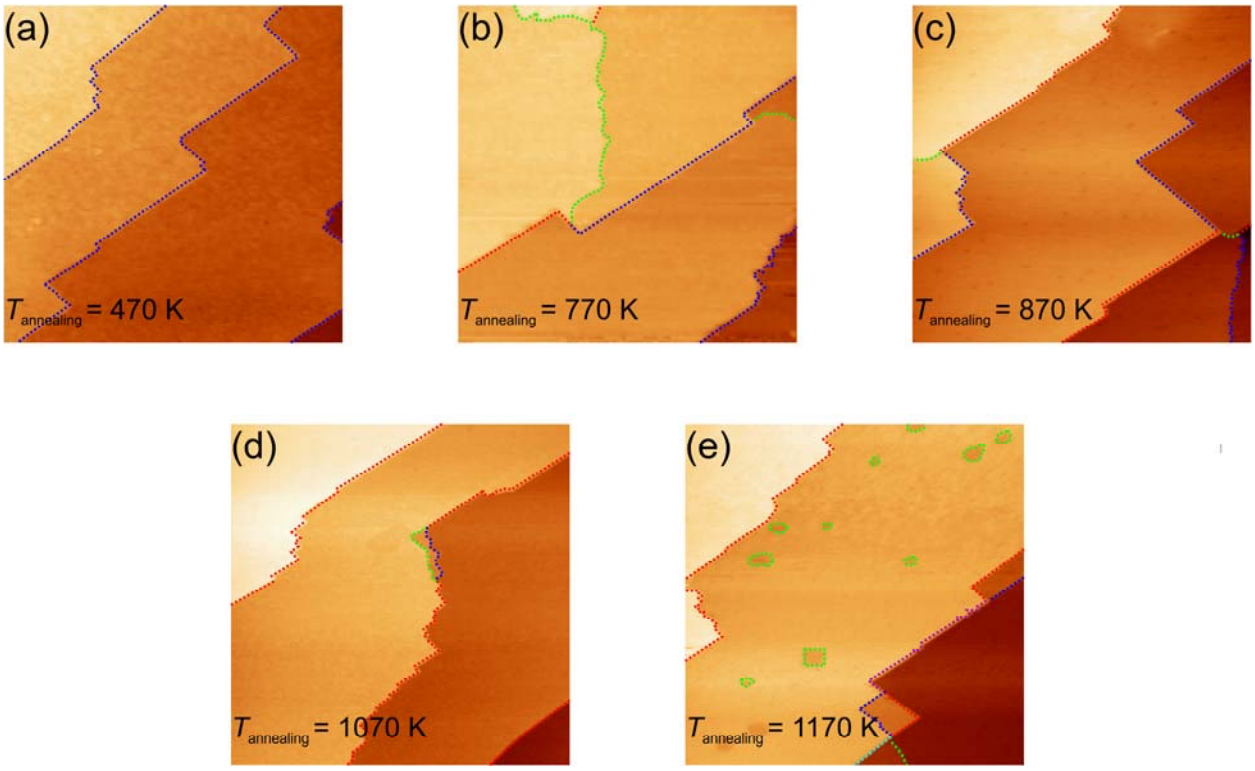

Figure 4: NC-AFM images illustrating the evolution of the surface morphology of a [100]-oriented $SrTiO_3$ single crystal sequentially annealed in UHV for 30 minutes to the temperatures indicated in the panels. Step heights evolve from unit cell step height (i.e., ≈4 Å; blue dotted lines) in (a) to a mixture between ½ (green dotted lines), 1, and 1½ unit cell step heights (red dotted lines) in (b) and (c) to almost exclusively 1½ unit cell step heights in (d). In (e), 2-Å deep holes start to appear, while elsewhere in the image steps featuring 2½ unit cell heights (cyan) have been formed. Image size is 500 × 500 nm^2 in all cases.

Let us note three important points. (1) Even though the data presented in Fig. 4 cover only a relatively small surface area, we have acquired data at different locations and repeated the same sequence with different crystals, all confirming the same trends. (2) The carbon

contamination is not a major factor since it will not introduce half unit cell high steps and the evolution of surface morphology was evident even when there was no trace of carbon in the AES spectra. (3) While it is apparent that an intermediate phase forms where most terraces are separated by 1½ unit cell steps, the exact nature of this phase remains unclear.

3.3 Evolution of Surface Roughness on Terraces as a Function of Annealing History

Having analyzed the height and shape of steps between terraces as a function of preparation history, we turn our attention to the surface's apparent roughness on individual terraces, calculated as described in the Experimental section, to gain insight into the local surface quality achieved under these conditions. Plotting data obtained by averaging roughness values from the image series described in Sect. 3.2 (Fig. 5), it is found that roughness is a non-monotonic function of the UHV annealing temperature, with the lowest values established between 900 K-1100 K.

To understand this behavior, let us recall that $SrTiO_3$ is nominally a good insulator, but its electrical properties can be tuned to semiconducting by doping.[62] Niobium doping, for example, provides electrons to the material's conduction band (*n*-doping). Similarly, oxygen deficiency induced by annealing pure $SrTiO_3$ in UHV,[33,44] also results in *n*-doping as each oxygen atom that is removed leaves two electrons behind that reduce the transition metal cations. For the annealing temperatures and durations investigated in this study, however, the conductivity of pure $SrTiO_3$ was too low to allow imaging by scanning tunneling microscopy (STM). Contrary to our expectations, the conductivity of the Nb-doped samples was similarly insufficient for STM operation without high-temperature annealing; in this context, we note that lower-than-specified

doping levels have previously been found.[62] As a result, charges could get 'trapped' near sub-surface Nb-dopants, oxygen vacancies, and more generally at all places where structural disorder (such as surface reconstruction domain boundaries) can accommodate local oxygen deficiency,[63] which causes the electrostatic component of the surface potential to become modulated at the nanometer scale.[27] Since NC-AFM images ultimately mirror the surface potential, such charge modulations appear as enhanced roughness.[27,28,30,41,64] Putting all of the pieces together, we therefore assign the initial decline in surface roughness at modest temperatures to improved surface ordering and eliminating surface contamination, while the subsequent increase for higher temperatures is likely a manifestation of the heightened charge disorder described above.

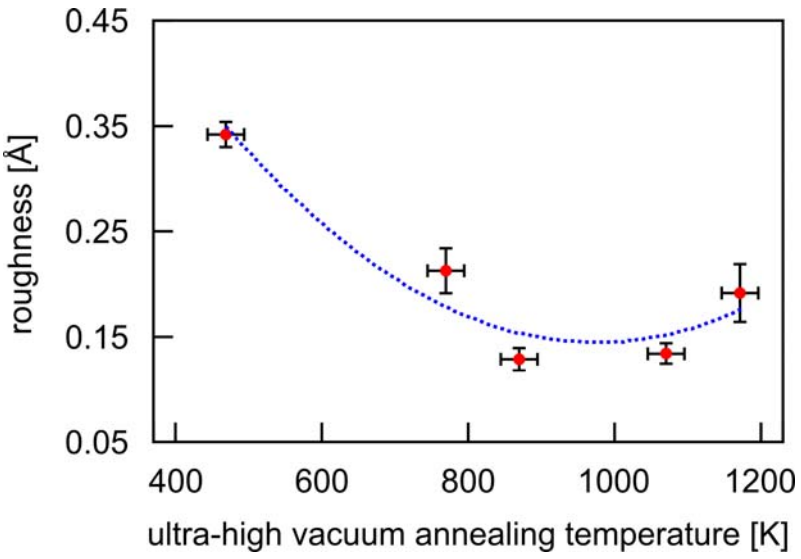

Figure 5: Root mean square surface roughness of $SrTiO_3$, as measured on otherwise 'atomically flat' terraces, plotted for different UHV annealing temperatures. After an initial sharp decrease, it is found to rise again for values above ≈1100 K.

3.4 Evolution of Surface Roughness on Terraces as a Function of Applied Bias Voltages

If charge disorder dominates the nanometer-scale contrast in the NC-AFM images rather than the actual atomic structure, we should be able to influence it by establishing a potential difference between the tip and the sample. Indeed, when we adjust the bias voltage applied to the $SrTiO_3$ crystal while the tip is grounded, we observed significant changes in the surface roughness as tracked by NC-AFM. An example of this effect is given in Fig. 6, where the 'apparent roughness' of an otherwise atomically flat terrace is seen to vary by more than a factor of 4 when the bias voltage was swept between ±800 mV. We note for context that (i) the effect is fully reversible; (ii) even though roughness values may vary, the general trend was mirrored by all samples we investigated, independent of their exact preparation procedure; and (iii) the sample shown in Fig. 6 had been imaged with a base pressure of 2×10^{-11} mbar, which rules out the effect of surface contamination over the time scale of the experiments.

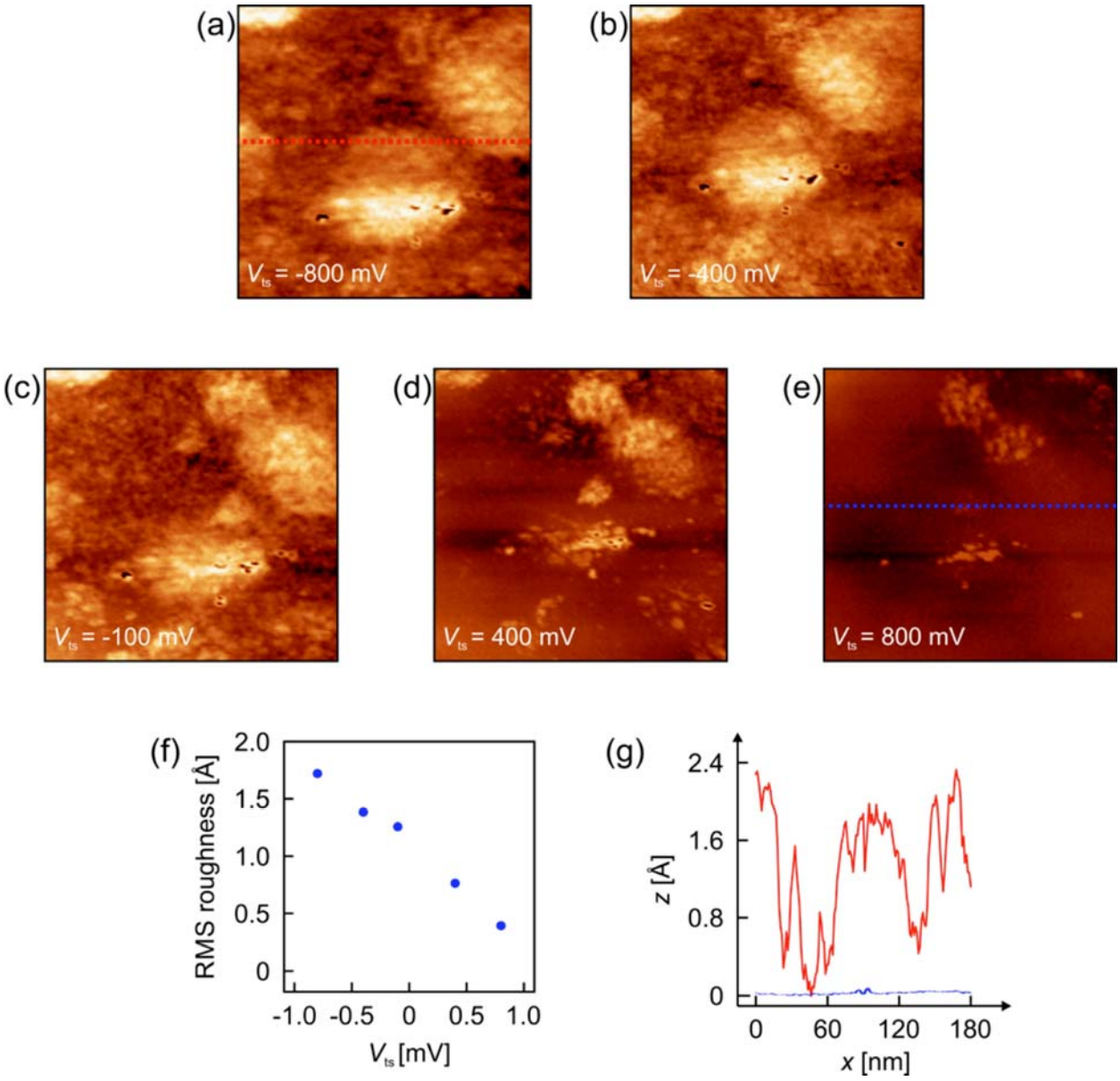

Figure 6: (a)-(e) NC-AFM images (180 nm × 180 nm) demonstrating substantial changes in the apparent surface roughness while ramping the bias voltage applied to the back of the crystal. All images cover the same *z* range of 4.8 Å from darkest color to brightest color. (f) Plot of the root mean square (RMS) surface roughness as a function of the applied bias voltage V_{ts}. (g) Cross sections along the lines highlighted in image (a) (red) and (e) (blue) visualizing the decrease in peak-to-peak roughness. The sample was a 0.7 % Nb-doped $SrTiO_3$ crystal that was prepared by heating in O_2 flow for 30 minutes to 1270 K followed by a 30 minutes anneal in UHV at 800 K. The minimum observed roughness (in (e)) is ≈0.4 Å, which is consistent with roughness data calculated from the terraces shown in Figure 4.

To explore this effect in more detail, we conducted bias sweep experiments with the tip confined to a single spot over the surface. To eliminate ambiguities that may arise from the simultaneous presence of Nb^{5+} and Ti^{3+} dopants, the latter introduced by reduction, we used Nb-free samples for these experiments. During each sweep, the feedback was active so that the *z* piezo reacted by extending and retracting to keep the total tip-sample interaction constant. From Fig. 7a, it becomes evident that the vertical position of the tip with respect to the surface, labeled as '*z* piezo' and arbitrarily calibrated to zero at the lowest value in the data, has a strong dependence on the applied bias voltage V_{ts} for values smaller than -0.7 V and larger than 1.2 V. This is because applying a negative bias voltage to the back of the sample drives the negative charge carriers (the conduction band electrons) out of the bulk causing them to *accumulate* at the surface while a positive image charge is induced at the tip apex (labeled as 'accumulation' in Fig. 7a). More specifically, the electric field due to the negative potential causes a downward band bending, which attracts the electrons towards the surface.[27,28,64] Conversely, when a positive bias is applied, electrons are pushed into the bulk through an 'upwards band bending,[28,64] while a negative image charge is induced at the tip apex ('inversion'); note that both regimes lead to an additional attractive force between tip and sample that causes the feedback to enlarge the distance between tip and sample, which results in larger *z*-piezo values. In addition, theoretical studies performed with perovskites indicate that oxygen may have a very small energy barrier for diffusion in defect-rich environments, which may induce some degree of oxygen mobility under the influence of the external field.[65,66]

From Fig. 7a, we also gather the existence of a well-expressed 'transition' region between -0.7 V and 1.2 V, where changes in the applied bias voltage affect the vertical position of the tip to a much lesser degree than within the accumulation and inversion regimes. This is

because when the reduced downward band bending causes the conduction band to increase above the Fermi level, only very few mobile charge carriers are available at the surface, and a 'depletion layer' emerges.[64] After crossing the 'flatband condition', the depletion layer becomes thicker until the valance band also crosses the Fermi level through upwards band bending and electrons from the valence band are pushed into the bulk. Zooming into that area (Fig. 7b), we see that the *z* piezo position as a function of applied bias voltage follows a roughly parabolic shape. Due to the different work functions of tip and sample, the minimum of the parabola is offset from zero ($V_{min} \approx$ -0.07 V) by the contact potential difference.

Based on the results from Fig. 7a & b, we have conducted bias sweep experiments along a scan line to check the local variation of the contact potential difference by determining V_{min} every 5 nm along a line of 200 nm length. From the data in Fig. 7c, we see that V_{min} fluctuates within that distance by ±400 mV. In fact, changes of ±200 mV from one data point to another are not uncommon, while the standard deviation of multiple measurements of V_{min} at the same position is only 8.5 mV. The autocorrelation function of the data in Fig. 7c decays by one data point, indicating uncorrelated fluctuations of V_{min} within a 5 nm distance. A statistical analysis of the discrete values of V_{min} is given in Fig. 7d; the blue line, indicating a Gaussian distribution, is added to guide the eye only. In any event, the local variation of V_{min} along a scan line causes the observed high values for the apparent roughness, thereby impeding atomic resolution imaging which requires a flat background over a roughly 5 nm × 5 nm area.

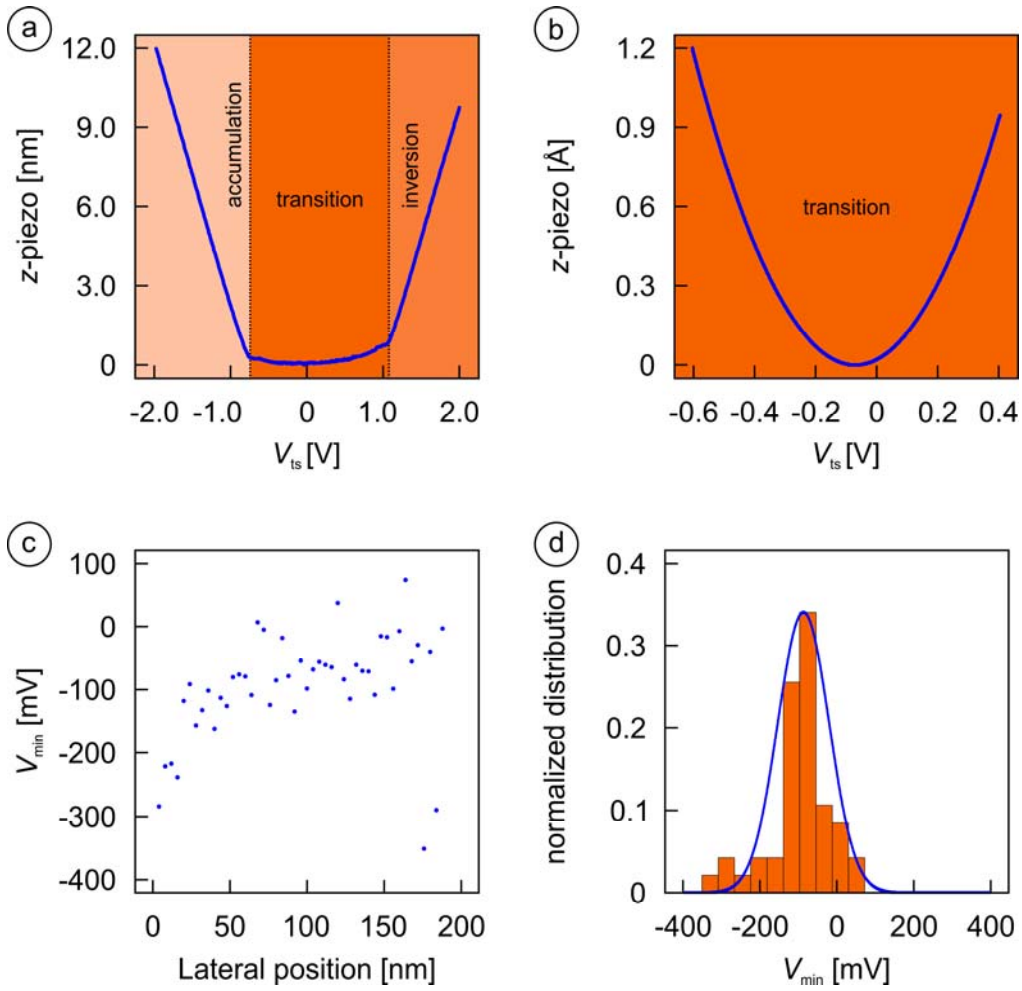

Figure 7: Results of bias sweep experiments conducted on undoped $SrTiO_3$, where the vertical position of the tip relative to the surface (labeled as '*z*-piezo') was recorded as a function of a bias voltage applied to the backside of the $SrTiO_3$ crystal. (a) *z*-piezo vs. bias voltage plot. Three different regions (accumulation, transition, and inversion) were observed when ramping the bias. (b) Zoom into the transition region. (c) Plot of V_{min}, representing the value of the applied bias voltage V_{ts} at the minimum of the parabola in the transition region, for bias sweeps carried out at 40 distinct lateral positions along a straight line with 5 nm spacing between individual points. (d) Normalized statistical distribution of the values plotted in (c); the blue line, which represents a Gaussian distribution, is added solely to guide the eye.

4. Discussion

The first part of this study related to the characterization of the evolution of surface terminations on $SrTiO_3$. All terminations encountered in this study ((√13×√13)-*R*33.7°, c(4×2), (4×4), (2×2),

and (2×1)) have been observed before, but two features stand out: First, we found LEED patterns reflecting the c(4×2) reconstruction during most of the preparation schemes applied, while before this specific surface termination was only seen after cycles of Ar sputtering. This is remarkable because Kienzle et al.[23] theoretically predict the c(4×2) to have a relatively high surface energy per (1×1) unit cell of ≈1.78 eV ((1×1)Ti: ≈1.38 eV; ((1×1)Sr: ≈1.29 eV). On the other hand, the (√13×√13)-*R*33.7° was found to have the lowest surface energy per unit cell of all surface terminations calculated (≈1.23 eV), which may explain why it was observed after prolonged annealing in oxygen rich environments. Let us also note that the c(4×2) → (√13×√13)-*R*33.7° transition observed at higher oxygen fluxes during heating was reversed upon annealing in UHV. Supported by the AES results of Fig. 3 and the results of Sect. 3.2, we conclude that initially titanium-rich surfaces display measurable increases in Sr concentration during UHV annealing that also deplete O from the surface.

In the second part of the study, we went on to uncover that despite the existence of well-developed LEED patterns, a substantial degree of disorder appears in NC-AFM images. The latter manifests as a considerable 'apparent surface roughness' that can be influenced by applying a bias voltage, eventually inducing substantial band bending of both the conductance and valance bands that causes accumulation and inversion regimes to occur. While these results must certainly be viewed in light of the fact that the conductivity was insufficient for STM measurements, it was striking that it was seen on all of the samples we investigated. Based on an analysis of recent literature, we speculate that we have a situation similar to that encountered by Ohsawa et al.,[67] who "found that a typical annealing for preparation of $SrTiO_3$ substrates, unexpectedly, resulted in a disordered surface on an atomic scale". Similarly, Silly et al.,[39] despite achieving atomic resolution, observed highly disordered surface terminations. Yet it

remains curious how surfaces that appear well ordered in electron diffraction experiments reveal no order in surface microscopy. This divergent view of the same surface reflects differences in the sensitivities of the two measurements. The LEED measurement emphasizes the atomic periodicity of the surface atoms with rapidly decaying contributions from sub-surface layers. In contrast, NC-AFM is sensitive to anything that produces a spatially varying force on the tip, including trapped charges that can be several nanometers below the surface.[68] Thus, NC-AFM reveals that even $SrTiO_3$ surfaces prepared using standard procedures that yield sharp electron diffraction patterns still contain plentiful surface and near surface defects that can trap charge. One reason why this is not seen in many of the images $SrTiO_3$ surface reconstructions acquired with STM is that when conductivity is high enough for STM, the material is so doped that there are plentiful electrons to screen these effects.

To put the importance of this finding further into context, let us recall that charged point defects that act as dopants modify not only the electronic properties of the surface, but have also been identified as important determinants of the properties of interfacial materials based on $SrTiO_3$ substrates. Examples for this material class include the superconducting properties in monolayer FeSe on $SrTiO_3$ [12,13] and the conducting properties of the two dimensional electronic gas at the $LaAlO_3/SrTiO_3$ interface.[69,70] Our use of NC-AFM to characterize the number density and spatial distribution of charged defects may therefore be helpful in correlating substrate preparation routes and charge states with the characteristics of devices made from such interfacial materials. Since external electric fields were shown to cause a band bending through which charge accumulation or depletion at the surface can be tuned, one may even speculate that applying such fields during growth may be able to alter the properties of films grown on top.

5. Conclusion

The structural phase transformation of $SrTiO_3$ (100) samples induced by following various preparation schemes was investigated using AES, LEED, and NC-AFM. LEED measurements reveal the existence of (√13×√13)-*R*33.7°, c(4×2), (4×4), (2×2), and (2×1) reconstructions, with the surface changing from c(4×2) to (√13×√13)-*R*33.7° upon heating while offering a surplus of oxygen. In contrast, a (√13×√13)-*R*33.7° → c(4×2) → (4×4)/(2×2)/(2×1) sequence is observed when annealing in UHV. Complementary AES and NC-AFM measurements show that originally singly-terminated $SrTiO_3$ (100) crystals prepared under oxidizing conditions are initially enriched in Ti at the surface but evolve towards a surface with half unit cell steps and a more stoichiometric Sr:Ti ratio when reduced in UHV. Ultimately, such effects may be responsible for the varying quality of thin films grown on $SrTiO_3$(100) substrates.

Acknowledgments

We thank Mathew S. J. Marshall, Subhasish Mandal, Devine Kumah, Sohrab Ismail-Beigi, and Sang-Wook Cheong for helpful discussions. Financial support from National Science Foundation through the Yale Materials Research Science and Engineering Center (grant No. MRSEC DMR-1119826) is gratefully acknowledged.

References

[1] R. Peng, X.P. Shen, X. Xie, H.C. Xu, S.Y. Tan, M. Xia, T. Zhang, H.Y. Cao, X.G. Gong, J.P. Hu, B.P. Xie, and D.L. Feng, Physical Review Letters **112**, 107001 (2014).

[2] D. Liu, W. Zhang, D. Mou, J. He, Y.-B. Ou, Q.-Y. Wang, Z. Li, L. Wang, L. Zhao, S. He, Y. Peng, X. Liu, C. Chen, L. Yu, G. Liu, X. Dong, J. Zhang, C. Chen, Z. Xu, J. Hu, X. Chen, X. Ma, Q. Xue, and X.J. Zhou, Nat Commun **3**, 931 (2012).

[3] K. Liu, Z.-Y. Lu and T. Xiang, Physical Review B **85**, 235123 (2012).

[4] M.-G. Han, M.S.J. Marshall, L. Wu, M.A. Schofield, T. Aoki, R. Twesten, J. Hoffman, F.J. Walker, C.H. Ahn, and Y. Zhu, Nat Commun **5**, (2014).

[5] C.J. Lu, Z.L. Wang, C. Kwon, and Q.X. Jia, Journal of Applied Physics **88**, 4032 (2000).

[6] Q. Gan, R.A. Rao, C.B. Eom, J.L. Garrett, and M. Lee, Applied Physics Letters **72**, 978 (1998).

[7] A. Grutter, F. Wong, E. Arenholz, M. Liberati, A. Vailionis, and Y. Suzuki, Applied Physics Letters **96**, 082509 (2010).

[8] H. Yang, M. Jain, N.A. Suvorova, H. Zhou, H.M. Luo, D.M. Feldmann, P.C. Dowden, R.F. DePaula, S.R. Foltyn, and Q.X. Jia, Applied Physics Letters **91**, 072911 (2007).

[9] W. Qing-Yan, L. Zhi, Z. Wen-Hao, Z. Zuo-Cheng, Z. Jin-Song, L. Wei, D. Hao, O. Yun-Bo, D. Peng, C. Kai, W. Jing, S. Can-Li, H. Ke, J. Jin-Feng, J. Shuai-Hua, W. Ya-Yu, W. Li-Li, C. Xi, M. Xu-Cun, and X. Qi-Kun, Chinese Physics Letters **29**, 037402 (2012).

[10] Z. Li, J.-P. Peng, H.-M. Zhang, W.-H. Zhang, H. Ding, P. Deng, K. Chang, C.-L. Song, S.-H. Ji, L. Wang, K. He, X. Chen, Q.-K. Xue, and X.-C. Ma, Journal of Physics: Condensed Matter **26**, 265002 (2014).

[11] S. He, J. He, W. Zhang, L. Zhao, D. Liu, X. Liu, D. Mou, Y.-B. Ou, Q.-Y. Wang, Z. Li, L. Wang, Y. Peng, Y. Liu, C. Chen, L. Yu, G. Liu, X. Dong, J. Zhang, C. Chen, Z. Xu, X. Chen, X. Ma, Q. Xue, and X.J. Zhou, Nat Mater **12**, 605 (2013).

[12] S. Tan, Y. Zhang, M. Xia, Z. Ye, F. Chen, X. Xie, R. Peng, D. Xu, Q. Fan, H. Xu, J. Jiang, T. Zhang, X. Lai, T. Xiang, J. Hu, B. Xie, and D. Feng, Nat Mater **12**, 634 (2013).

[13] Q.-Y. Wang, Z. Li, W.-H. Zhang, Z.-C. Zhang, J.-S. Zhang, W. Li, H. Ding, Y.-B. Ou, P. Deng, K. Chang, J. Wen, C.-L. Song, K. He, J.-F. Jia, S.-H. Ji, Y.-Y. Wang, L.-L. Wang, X. Chen, X.-C. Ma, and Q.-K. Xue, Chinese Physics Letters **29**, 037402 (2012).

[14] M. Kawasaki, K. Takahashi, T. Maeda, R. Tsuchiya, M. Shinohara, O. Ishiyama, T. Yonezawa, M. Yoshimoto, and H. Koinuma, Science **266**, 1540 (1994).

[15] N. Bickel, G. Schmidt, K. Heinz, and K. Müller, Physical Review Letters **62**, 2009 (1989).

[16] T. Kubo and H. Nozoye, Surface Science **542**, 177 (2003).

[17] T. Nakamura, H. Inada, and M. Iiyama, Applied Surface Science **130–132**, 576 (1998).

[18] N. Erdman, K.R. Poeppelmeier, M. Asta, O. Warschkow, D.E. Ellis, and L.D. Marks, Nature **419**, 55 (2002).

[19] S. Gerhold, Z. Wang, M. Schmid, and U. Diebold, Surface Science **621**, L1 (2014).

[20] M.R. Castell, Surface Science **505**, 1 (2002).

[21] T. Kubo, H. Orita, and H. Nozoye, Physical Chemistry Chemical Physics **13**, 16516 (2011).

[22] N. Erdman and L.D. Marks, Surface Science **526**, 107 (2003).

[23] D.M. Kienzle, A.E. Becerra-Toledo, and L.D. Marks, Physical Review Letters **106**, 176102 (2011).

[24] A.P. Kajdos, and S. Stemmer, Applied Physics Letters **105**, 191901 (2014).

[25] K. Iwahori, S. Watanabe, M. Kawai, K. Mizuno, K. Sasaki, and M. Yoshimoto, Journal of Applied Physics **88**, 7099 (2000).

[26] M.R. Castell, Surface Science **516**, 33 (2002).

[27] T. Kubo and H. Nozoye, Appl Phys A **72**, S277 (2001).

[28] W. Sitaputra, N. Sivadas, M. Skowronski, D. Xiao, and R.M. Feenstra, Physical Review B **91**, 205408 (2015).

[29] B. Psiuk, J. Szade, H. Schroeder, H. Haselier, M. Mlynarczyk, R. Waser and K. Szot, Applied Physics a-Materials Science & Processing **89**, 451 (2007).
[30] Y. Liang and D.A. Bonnell, Surface Science Letters **285**, L510 (1993).
[31] M. Naito and H. Sato, Physica C: Superconductivity **229**, 1 (1994).
[32] Q. Jiang and J. Zegenhagen, Surface Science **367**, L42 (1996).
[33] Q.D. Jiang and J. Zegenhagen, Surface Science **425**, 343 (1999).
[34] B. Cord and R. Courths, Surface Science **162**, 34 (1985).
[35] R. Shimizu, K. Iwaya, T. Ohsawa, S. Shiraki, T. Hasegawa, T. Hashizume, and T. Hitosugi, ACS Nano **5**, 7967 (2011).
[36] P.J. Møller, S.A. Komolov, and E.F. Lazneva, Surface Science **425**, 15 (1999).
[37] T. Nishimura, A. Ikeda, H. Namba, T. Morishita, and Y. Kido, Surface Science **421**, 273 (1999).
[38] H. Tanaka, T. Matsumoto, T. Kawai, and S. Kawai, Japanese Journal of Applied Physics **32**, 1405 (1993).
[39] F. Silly, D.T. Newell, and M.R. Castell, Surface Science **600**, 219 (2006).
[40] K. Johnston, M.R. Castell, A.T. Paxton, and M.W. Finnis, Physical Review B **70**, 12 (2004).
[41] Y. Liang and D.A. Bonnell, Surface Science **310**, 128 (1994).
[42] T. Matsumoto, H. Tanaka, T. Kawai, and S. Kawai, Surface Science Letters **278**, L153 (1992).
[43] C.H. Lanier, A. van de Walle, E. Erdman, E. Landree, O. Warschkow, A. Kazimirov, and K.R. Poeppelmeier, J. Zegenhagent, M. Asta, L.D. Marks, Physical Review B **9**, (2007).
[44] R. Shimizu, K. Iwaya, T. Ohsawa, S. Shiraki, T. Hasegawa, T. Hashizume, and T. Hitosugi, Applied Physics Letters **100**, 263106 (2012).
[45] Y. Cao, S. Wang, S. Liu, Q. Guo, and J. Guo, The Journal of Chemical Physics **137**, 044701 (2012)
[46] R. Herger, P.R. Willmott, O. Bunk, C.M. Schlepütz, B.D. Patterson, and B. Delley, Physical Review Letters **98**, 076102 (2007).
[47] A.M. Kolpak, D. Li, R. Shao, A.M. Rappe, and D.A. Bonnell, Physical Review Letters **101**, 036102 (2008).
[48] K. Sudoh and H. Iwasaki, Surface Science **557**, L151 (2004).
[49] D.T. Newell, A. Harrison, F. Silly, and M.R. Castell, Physical Review B **75**, 205429 (2007).
[50] G. Binnig, Atomic Force Microscope and Method for Imaging Surfaces with Atomic Resolution, U.S. Patent US4724318 A, (1986).
[51] G. Binnig, C.F. Quate, and C. Gerber, Physical Review Letters **56**, 930 (1986).
[52] G. Binnig, H. Rohrer, C. Gerber, and E. Weibel, Physical Review Letters **49**, 57 (1982).
[53] R. Wiesendanger, *Scanning Probe Microscopy and Spectroscopy: Methods and Applications* (Cambridge University Press, 1994).
[54] B.J. Albers, M. Liebmann, T.C. Schwendemann, M.Z. Baykara, M. Heyde, M. Salmeron, E.I. Altman, and U.D. Schwarz, Review of Scientific Instruments **79**, (2008).
[55] A.J. Melmed, (AVS, Boston, Massachusetts (USA), 1991), pp. 601.
[56] F.J. Giessibl, Applied Physics Letters **73**, 3956 (1998).
[57] E.D. Omur, G. Jan, H. Hendrik, I.A. Eric, and D.S. Udo, Nanotechnology **27**, 065703 (2016).
[58] M. Li and E.I. Altman, Physical Review B **66**, 115313 (2002).
[59] M. Kareev, S. Prosandeev, J. Liu, C. Gan, A. Kareev, J.W. Freeland, M. Xiao, and J. Chakhalian, Applied Physics Letters **93**, 061909 (2008).
[60] R.J.D. Tilley, Journal of Solid State Chemistry **21,** 293 (1977).
[61] C.M. Brooks, R.B. Wilson, A. Schäfer, J.A. Mundy, M.E. Holtz, D.A. Muller, J. Schubert, D.G. Cahill, and D.G. Schlom, Applied Physics Letters **107**, 051902 (2015).
[62] M.S.J. Marshall, D.T. Newell, D.J. Payne, R.G. Egdell, and M.R. Castell, Physical Review B **83**, 035410 (2011).
[63] R.F. Klie, Y. Ito, S. Stemmer, and N.D. Browning, Ultramicroscopy **86**, 289 (2001).

[64] A. Schwarz, W. Allers, and U.D. Schwarz, R. Wiesendanger, Physical Review B **62**, 13617 (2000).
[65] D.A. Freedman, D. Roundy, and T.A. Arias, Physical Review B **80**, 064108 (2009).
[66] P. Erhart, P. Träskelin, and K. Albe, Physical Review B **88**, 024107 (2013).
[67] T. Ohsawa, K. Iwaya, R. Shimizu, T. Hashizume, and T. Hitosugi, Journal of Applied Physics **108**, 073710 (2010).
[68] E.I. Altman, M.Z. Baykara, and U.D. Schwarz, Accounts of Chemical Research **48**, 2640 (2015).
[69] A.D. Caviglia, S. Gariglio, N. Reyren, D. Jaccard, T. Schneider, M. Gabay, S. Thiel, G. Hammerl, J. Mannhart, and J.M. Triscone, Nature **456,** 624 (2008).
[70] T. Ohnishi, K. Shibuya, T. Yamamoto, and M. Lippmaa, Journal of Applied Physics **103**, 103703 (2008).